Energy Proceedings
Vol 31, 2023
ISSN 2004-2965

Large-sized nanofilm-constructed hierarchical porous g-C_3N_4/SiO_2 with enhanced visible-light-driven photoactivity

Zhiyu Zhang [1], Yunxiao Liang [2*], Yong Ren [1*]

1 Department of Mechanical, Materials and Manufacturing Engineering, University of Nottingham Ningbo China, Ningbo 315100, China. Email: yong.ren@nottingham.edu.cn

2 State Key Laboratory Base of Novel Functional Materials and Preparation Science, School of Materials Science and Chemical Engineering, Ningbo University, Ningbo, 315211, China. Email: liangyunxiao@nbu.edu.cn

ABSTRACT

Novel large-sized nanofilm-constructed hierarchical porous SiO_2 (macropore size of 0.5–1.0 μm, wall thickness of 40–50 nm) was prepared by a dual-templating approach, and used as the advanced support for g-C_3N_4 photocatalyst. The photocatalytic activities were evaluated by degradations of Rhodamine B (RhB) under the simulated sunlight irradiation and experiments were conducted at wide ranges of the g-C_3N_4 loading content, solution pH, and photocatalyst dosage. The combination of increased light absorption, improved electron–hole separation and adsorption capacity, endows this fine structure with excellent photocatalytic performance. The trapping experiments were also performed to identify the main reactive species in the catalytic reactions.

Keywords: mesoporous nanofilm, hierarchical porous silica, graphitic carbon nitride, degradation of organic pollutant, wastewater emission reduction

1. INTRODUCTION

Due to the increasingly environmental crisis around the world, providing a possible method for renewable energy generation is necessary. Graphitic carbon nitride (g-C_3N_4), as a typical semiconductor photocatalyst, has gained wide interest resulting from its outstanding properties including great stability, visible light absorption, suitable conduction band position and facile preparation [1-3]. However, pristine g-C_3N_4 made from direct calcination of precursor exhibits unsatisfactory photocatalytic performance because of rapid electron-hole recombination and exposed limited active sites. Therefore, many strategies such as coupling with other semiconductors [2, 4], doping with metal or nonmetal elements [5-6], modification with noble metal nanoparticles [3, 7], etc, have been explored to enhance the visible light photocatalytic performance of g-C_3N_4. Apart from that, delaminating bulk g-C_3N_4 into g-C_3N_4 nanosheets has been regarded as one of effective ways to improve charge transfer. Unfortunately, g-C_3N_4 nanosheets are inclined to aggregate because of inevitable strong van der Waals force-induced adhesion between layers. The problem of g-C_3N_4 nanosheets aggregation can be efficiently mitigated by constructing 3D structures. Moreover, the introduce of 3D hierarchical porous structures can enhance the photocatalytic performance of g-C_3N_4 benefited from high specific surface area, excellent light absorption and fast mass transport process.

However, g-C_3N_4 is usually used as a powder material in practical applications, means that the main drawbacks of powder materials are urgently required to be resolved: recycle difficulty, easy aggregation and possible secondary pollution of powder nanomaterials. In practical applications, macroscopic materials are much easier to manipulate and process [8-9], which could solve the problem of difficult recycle. Among different materials, macroscopic SiO_2 is easy preparation and highly thermal stable, which make it suitable to be an ideal candidate to support g-C_3N_4 by calcination for great performance.

Herein, we developed a new strategy for the preparation of novel g-C_3N_4/SiO_2 photocatalysts, which exhibited high photoactivity toward pollutant molecule decomposition under visible light irradiation. Firstly, large-sized nanofilm-constructed hierarchical porous SiO_2 (LNCHPS) with two sets of well-defined 3D continuous pass-through macropores was successfully synthesized by using dual-templating method. Subsequently, g-C_3N_4 was deposited uniformly onto the surface of LNCHPS. The presence of continuous pass-through macropores facilitates matter transport; meanwhile incident light can scatter within the macropore channels, increasing the utilization of light. Moreover, mesopores with short pore channel could facilitate the adsorption of pollutants and increase the specific surface area of SiO_2. Detailed experiments were performed to elucidate the effects of g-C_3N_4 loading content, solution pH and photocatalyst dosage. In the end, photogenerated active species were identified in the catalytic reactions.

2. EXPERIMENTAL DETAILS

2.1 Materials

All chemicals were of analytical grade and used without further purification. Deionized water was used in all synthesis and treatment processes. Polyethylene glycol 20000 (PEG 20000) was obtained from Tianjin Fengchuan Co., Ltd. Ethylsilicate (TEOS), urea, tert-butyl alcohol (TBA), benzoquinone (BQ) and potassium iodide (KI) were purchased from Macklin. Pluronic F127 ($PEO_{106}PPO_{70}PEO_{106}$) was obtained from Hangzhou Nathmay Nano Material Co., Ltd. Rhodamine B (RhB) was supplied by Beijing Chemical Reagent Research Institute.

2.2 Synthesis

2.2.1 Synthesis of LNCHPS

Firstly, monolithic macroporous polymers were synthesized according to the literature procedure [10], and then used as hard template. TEOS and F127 were utilized as a source of silicon and mesoporous porogen, respectively. In brief, 5.0 mL TEOS, 0.42 g F127 and 0.046 mL HNO_3 (68 wt%) were added into 10 mL deionized water with vigorous stirring for 2 h. Then the macroporous polymer templates were immersed in the solution and maintained on a shaker for 5 h, and subsequently placed in an oven at 40 °C for 24 h. At last, the products were calcined at 600 °C for 2 h (heating rate: 5 °C min^{-1}). The shape of the resulting hierarchical porous SiO_2 was generally made into rectangle in this work.

2.2.2 Synthesis of g-C_3N_4/LNCHPS

g-C_3N_4/LNCHPS was fabricated through a very simple dipping method and a subsequent calcination at high temperature. Specifically, a certain amount of urea was added into 15 mL deionized water, then dropped in HCl (36 wt%) to keep the pH value within 4.0–5.0. Then the prepared SiO_2 was immersed in the above mixture for 5 h. Subsequently, place the completely impregnated product in the oven at 60 °C for 12 h. At last, the precursor was placed in a covered crucible and calcined at 550 °C for 2 h (heating rate: 10 °C min^{-1}) in a muffle furnace.

In this procedure, the g-C_3N_4 content was modified by adding different amounts of urea and the photocatalysts are hereafter referred to as CNS-w for the samples fabricated from different conditions. The 'w' represents the g-C_3N_4 content (12.8, 16.0, 18.9, 23.5 wt%), while the pure macro-mesoporous SiO_2 is denoted as S_0.

2.3 Sample characterization

The g-C_3N_4 content was determined by Vario EL cube Organic Element Analyzer (OEA). An AXS-D8 ADVANCE X-ray powder diffractometer (Cu Kα, λ = 0.154 nm, 40 kV, 200 mA) was used to record X-ray diffraction (XRD) patterns of all samples ranging from 10 to 70° (2θ). The Fourier transform infrared (FTIR) spectra were characterized via PEOTEGE460 E.S.P Fourier transform infrared spectrometer. The morphologies of the samples were observed by an S-4800 scanning electron microscope (SEM). Nitrogen adsorption-desorption isotherms were recorded using a V-Sorb 2800P surface area and aperture analyzer to study the pore volume and pore-size distribution. The UV-vis absorption spectra of the as-prepared photocatalytsts were measured by a Lambda 950 UV-vis spectrophotometer (USA) with $BaSO_4$ as the reflectance standard.

2.4 Photodegradation experiment

The activities of the as-prepared catalysts for photodegradation of RhB under visible-light irradiation were measured with a 250 W Xe lamp containing an ultraviolet cutoff filter (> 400 nm) as the visible-light source. The RhB photodegradation experiments were carried out with 20 mg of the as-prepared catalyst

suspended in 20 mL of 10 mg/L RhB aqueous solution with constant magnetic stirring for 1 h in the dark to reach the adsorption equilibrium. Then the RhB mixture containing the photocatalysts was irradiated. At 30 min intervals, a 3 mL portion of the solution was taken out and analyzed directly for the concentration of residual RhB by UV-vis spectroscopy at a wavelength of 552 nm. The degradation efficiency of the photocatalysts was taken as the average results of three tests. Hydrochloric acid (HCl) was used to adjust the original pH values of the system.

3. RESULTS AND DISCUSSION

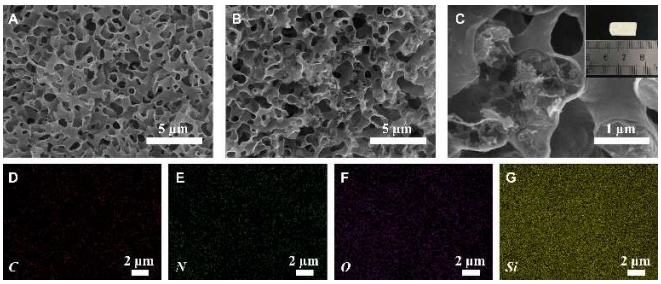

Fig. 1 SEM images of LNCHPS (A); g-C_3N_4/LNCHPS (B,C); digital photograph of g-C_3N_4/LNCHPS (inset in C); element mapping images for g-C_3N_4/LNCHPS (D-G).

The SEM images of LNCHPS and the typical g-C_3N_4/LNCHPS are shown in Fig. 1. The silica precursors generated from the hydrolysis of TEOS assembled with F127 micelles and then uniformly attached onto the surface of the macroporous polymer skeleton by electrostatic and hydrogen bonding interactions, growing into a nanofilm. After aging and calcining, the templates were removed, forming a monolithic macroporous material constructed of mesoporous SiO_2 nanofilm, as shown in Fig. 1A. LNCHPS has 3D interconnected macroporous channels with the wall thickness ranging from 40 to 50 nm. The mesopores existed in the macropore wall have a very short diffusion path. Compared to a micron-sized diffusion length, such as that in the conventional SBA-15, the typical diffusion time scale τ is then significantly shortened in g-C_3N_4/LNCHPS ($\tau = l^2/2D$, l is the diffusion length and D is the diffusion coefficient) [11], which could be regarded as an outstanding characteristic of the prepared photocatalyst. Some wrinkle shaped nanosheets can be clearly observed on the surface of SiO_2 nano-film, indicating the successful preparation of g-C_3N_4 nanosheets (Fig. 1B). The g-C_3N_4 should exist in a few layers, which is consistent with the following results of XRD. In this structure, the g-C_3N_4 nanosheet and LNCHPS have sufficient contact interface. Meanwhile, the decoration of g-C_3N_4 on SiO_2 surface was achieved by high temperature pyrolysis process. Thus we speculate that the g-C_3N_4 nanosheets possess high stability on the surface and cannot fall down easily. Furthermore, the tight attachment can prevent the g-C_3N_4 nanosheets aggregating effectively during the use procedure. Fig. 1C inset shows the digital photograph of g-C_3N_4/LNCHPS, which maintains the original exterior of LNCHPS. The size of material is adjustable to meet different needs of applications. The corresponding element mapping image presents the microcosmic uniform distribution of C, N, O, and Si in g-C_3N_4/LNCHPS (Fig. 1D – G).

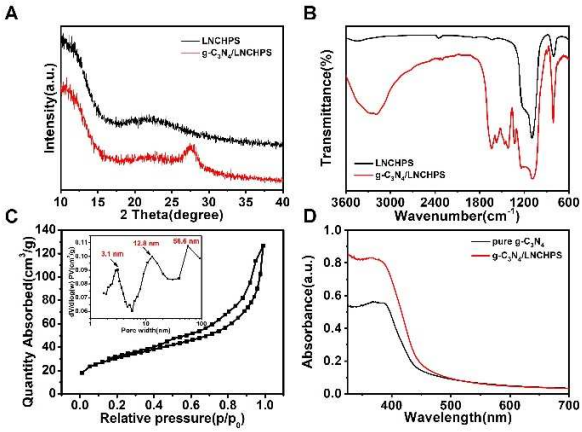

Fig. 2 XRD patterns of LNCHPS and g-C_3N_4/LNCHPS (A); FT-IR spectra of LNCHPS and g-C_3N_4/LNCHPS (B); nitrogen adsorption-desorption isotherm of g-C_3N_4/LNCHPS (C) and mesopore distribution of g-C_3N_4/LNCHPS (inset in C); UV-Vis spectra of pure g-C_3N_4 and g-C_3N_4/LNCHPS (D).

Fig. 2A shows the XRD patterns of the LNCHPS and g-C_3N_4/LNCHPS. A broad signal around 22° in LNCHPS is assigned to the amorphous silica. The diffraction peak at 27.5° can be assigned to the (002) planes and suggests that g-C_3N_4 has successfully been immobilized on the SiO_2.

Fig. 2B shows the Fourier transform infrared (FT-IR) spectra of LNCHPS and g-C_3N_4/LNCHPS. The band at 1648 cm^{-1} is assigned to the typical C=N stretching vibration. The bands corresponding to the C-N stretching appear at 1243, 1319, and 1430 cm^{-1}. The characteristic peak at 808 cm^{-1} is attributed to the triazine rings, suggesting the formation of the typical structure of g-C_3N_4.

Fig. 2C shows the N_2 adsorption-desorption isotherm of g-C_3N_4/LNCHPS. It exhibits type IV isotherm and the shape of the hysteresis loop is of Type H3, indicating the presence of mesopores. The pore size

distribution curve (insert of Fig. 2C) also proves this result. In addition, the channel length of these mesopores in the macropore wall (silica nanofilm) is quite short (about several tens of nanometers), significantly improving the efficiency of mass diffusion compared with mesoporous silica with channels of micro-scale length. The BET specific surface area is measured to be 107.3 $m^2 \cdot g^{-1}$, which will provide more reaction active sites for photocatalysis.

Fig. 2D shows the UV-vis diffuse reflectance spectra (DRS). The absorption wavelength of pure g-C_3N_4 is around 450 nm, attributing to the intrinsic band gap (about 2.7 eV). It is noted that the extended absorbance of g-C_3N_4/LNCHPS seems broader than that of pure g-C_3N_4, which implies improved absorption of visible light. It can be inferred that the porous structure can promote the multiple reflection of incident light, which would be beneficial to show the better activity in the photocatalytic process.

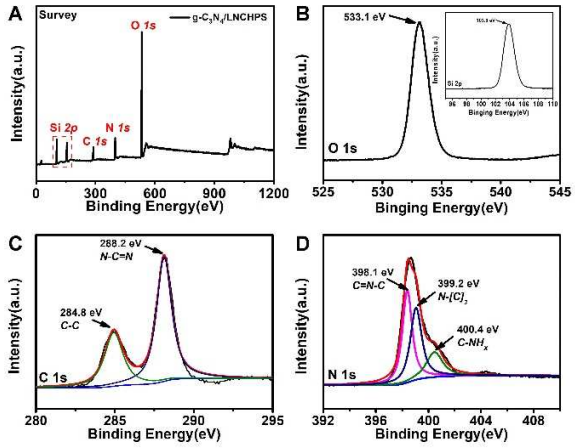

Fig. 3 XPS survey spectrum of g-C_3N_4/LNCHPS (A); O 1s XPS spectrum (B), Si 2p XPS spectrum (inset in B); C 1s XPS spectrum (C); N 1s XPS spectrum (D).

The high resolution XPS spectra were acquired to analyze the chemical composition and the element chemical status of the g-C_3N_4/LNCHPS. As exhibited in Fig. 3A, four elements of C, N, O and Si are all found. In Fig. 3B, the peak located at the binding energy of 533.1 eV can be assigned to the O^{2-} in the SiO_2. Inset displays the XPS spectrum of Si 2p with the characteristic peak at the binding energy of 103.9 eV, corresponding to the state of Si^{4+} in SiO_2. The C 1s spectrum in Fig. 3C can be separated into two peaks centered at 284.8 and 288.2 eV, respectively. The peak at 284.8 eV is ascribed to the C–C bonds, while the peak at 288.2 eV is assigned to sp^2-bonded carbon in N-containing aromatic structure (N–C=N). The N 1s curve is deconvolved into three peaks locating at 398.1, 399.2 and 400.4 eV (Fig. 3D). The peak located at 398.1 eV is commonly ascribed to the sp^2-bonded N involved in the triazine rings (C–N=C) dominated in the g-C_3N_4. The peaks located at 399.2 and 400.4 eV can be assigned to the tertiary N in N–$(C)_3$ units and amino groups with a hydrogen atom (C–N–H), respectively. These XPS spectra confirm the basic heptazine heterocyclic structure of g-C_3N_4 on LNCHPS.

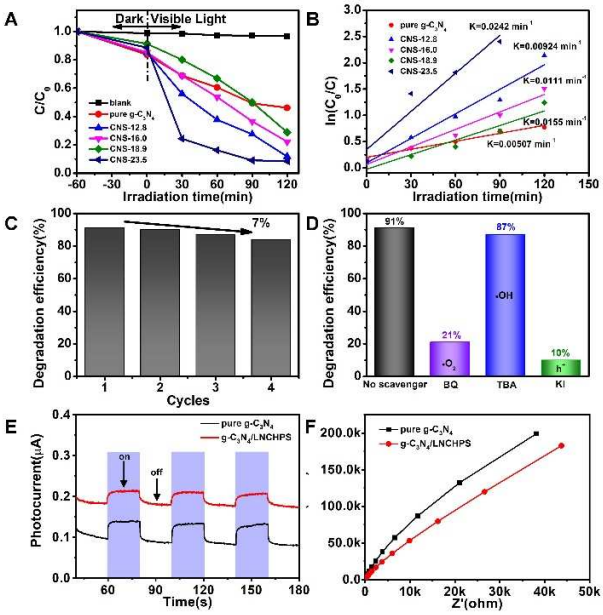

Fig. 4 Photocatalytic degradation of RhB in the presence of pure g-C_3N_4 and a series of g-C_3N_4/LNCHPS under visible-light irradiation (A) together with corresponding kinetic fitting curves (B); reusability of g-C_3N_4/LNCHPS-15 for RhB degradation (C); effects of radical trapping by various scavengers on the photodegradation of RhB (D); transient photocurrent responses of pure g-C_3N_4 and g-C_3N_4/LNCHPS (E); electrochemical impedance spectroscopy of pure g-C_3N_4 and g-C_3N_4/LNCHPS (F).

RhB is one of common dyes in industrial processes and was degraded under visible light irradiation to evaluate the photocatalytic activity of the photocatalyst. As shown in Fig. 4A, RhB can be only slightly degraded without photocatalysts and g-C_3N_4 content plays an important role in the reaction. In Fig. 4B, the rate constant reached the peak value at 0.0242 min^{-1} when the g-C_3N_4 content was 23.5 wt%, which was 4.8 times that of pure g-C_3N_4. Two factors: the specific surface area and total g-C_3N_4 content would account for the reason. When the g-C_3N_4 content is low, the photocatalyst with high specific surface area and absorption capacity exhibits better performance. When

the g-C_3N_4 content is quite high, the excessive g-C_3N_4 loading provides the SiO_2 matrix with abundant active sites, thus resulting in the best photoactivity. Photocatalytic experiments with different pH values were also carried out in RhB aqueous solution. According to the results, photocatalysts remain highly effective activity between 1.0 and 9.0, among which the pH value of 3.0 was the optimal condition, indicating that the acidic condition was obviously favorable. The RhB molecule possesses a positive charge, which is more favorable for the adsorption of RhB molecules in an acidic solution. Therefore, the amount of absorbed reactant increased and the photodegradation rate was enhanced accordingly. Besides, the effect of catalyst dosage was also investigated. The photocatalytic efficiency increased continuously as the catalyst dosage increased from 0.1 to 2.0 g/L. Usually, catalysts used in the form of powders have a threshold in aqueous suspension system. However, the good transparency of LNCHPS can avoid the cover of light and a difficult radiation pentration in the solution. Apart from that, in UV-vis spectra, the absorption peak locating at 552 nm rapidly decreased with the extension of irradiation time, indicating a rapid decomposition of RhB molecules. This result was in good connection with gradual color variation of the solution.

The reusability experiments were performed and the degradation efficiency recorded after 4 cycles are shown in Fig. 4C. There was a slight decrease in photocatalytic activity appeared in the fourth cycle, thus demonstrating the superior reusability. In addition, the catalyst could be separated without extra centrifugation, avoiding the problem of loss.

In order to further understand the photocatalytic mechanism, controlled experiments with adding different scavengers had been performed. Fig. 4D shows the photocatalytic activities in presence of different scavengers, i.e., BQ scavenger for $\bullet O_2^-$, TBA scavenger for •OH and KI scavenger for holes, respectively [12]. The degradation of RhB could be inhibited by the addition of scavengers and these results clearly suggested that $\bullet O_2^-$, •OH and h^+ were all the active species. When KI was added, the degradation rate of RhB obviously decreased, suggesting that h^+ was the most critical reactive species. In contrast, •OH played a relatively minor role [13]. In the procedure, O_2 molecules could react with e^- to generate $\bullet O_2^-$ and active •OH was produced by h^+ and OH^-/H_2O. $\bullet O_2^-$ and h^+ were powerful oxidizing agents, which could attack RhB molecules and finally degraded them into H_2O and CO_2. The major reaction processes in this photodegradation of RhB were described as follows:

g-C_3N_4/LNCHPS + hν→g-C_3N_4 (e^- + h^+)/LNCHPS (1)

e^- + O_2→$\bullet O_2^-$ (2)

$\bullet O_2^-$, h^+ + RhB→CO_2 + H_2O (3)

Transient photocurrent response curves and electrochemical impedance spectroscopy (EIS) were used to investigate the interfacial charge transfer behaviors [14]. Fig. 5A shows the photocurrent-time signals for as-prepared samples under several on-off cycles of illumination (λ > 420 nm). Due to the rapid recombination of photo-generated electron-hole pairs, pure g-C_3N_4 shows the lower current density. The improved photocurrent density of g-C_3N_4/LNCHPS validates that 3D porous structures can endow g-C_3N_4 with highly efficient electron transfer. Besides, EIS analysis was carried out to get further information on the charge transfer process [15]. The radius of arc in Fig. 5B is generally connected with the resistance at the electrode-electrolyte interface, and a shorter arc radius represents a lower charge transfer resistance[57,58], implying a higher interfacial charge transfer rate in g-C_3N_4/LNCHPS. Photoluminescence (PL) technique was also used to investigate the property of radiative recombination process. Pure g-C_3N_4 possesses a stronger emission peak at 440 nm owing to the radiative recombination effect of self-trapped excitons. In contrast, g-C_3N_4/LNCHPS can profit from 3D porous structures, elevating the dissociation efficiency of excitons and inhibiting the recombination of charge carriers.

4. CONCLUSIONS

In summary, novel large-sized nanofilm-constructed hierarchical porous SiO_2 (LNCHPS) was successfully synthesized, and then g-C_3N_4 were immobilized on the surface of it via a simple impregnation method. LNCHPS possesses well-defined 3D continuous pass-through macropores and abundant mesopores in the macropore wall. g-C_3N_4/LNCHPS exhibited excellent photocatalytic activity in the degradation of RhB compared to pure g-C_3N_4 as well as high stability and very easy recovery. The reasons for this enhancement performance can be ascribed to a hierarchical porous structure, which can boost light absorption ability resulting from multiple reflection effects, improved charge carrier mobility and adsorption capacity.

ACKNOWLEDGEMENT

This work was financially supported by the Science and Technology Benefiting Projects of Ningbo (Grant No. 2017C50033), the Public Projects of Zhejiang Province (Grant No. LGG19E020002), and KC Wong Happiness Fund in Ningbo University. The authors would like to acknowledge the support from the Ningbo Municipal Key Laboratory on Clean Energy Conversion Technologies (2014A22010) as well as the Zhejiang Provincial Key Laboratory for Carbonaceous Wastes Processing and Process Intensification Research funded by the Zhejiang Provincial Department of Science and Technology (2020E10018).

REFERENCE

[1] Mo Z, Xu H, Chen Z, et al. Self-assembled synthesis of defect-engineered graphitic carbon nitride nanotubes for efficient conversion of solar energy. Applied Catalysis B: Environmental, 2018, 225: 154–161.

[2] Hao R, Wang G, Tang H, et al. Template-free preparation of macro/mesoporous g-C_3N_4/TiO_2 heterojunction photocatalysts with enhanced visible light photocatalytic activity. Applied Catalysis B: Environmental, 2016, 187: 47–58.

[3] Zhou X, Zhang G, Shao C, et al. Fabrication of g-C_3N_4/SiO_2-Au composite nanofibers with enhanced visible photocatalytic activity. Ceramics International, 2017, 43: 15699–15707.

[4] Jia H, Ma D, Zhong S, et al. Boosting photocatalytic activity under visible-light by creation of PCN-222/g-C_3N_4 heterojunctions. Chemical Engineering Journal, 2019, 368: 165–174.

[5] Sun F, Xu C, Yu Y, et al. Carbon self-doping induced activation of n–p* electronic transitions of g-C_3N_4 nanosheets for efficient photocatalytic H_2 evolution. ChemCatChem, 2016, 8: 3527–3535.

[6] Zhou C, Lai C, Xu P, et al. Rational design of carbon-doped carbon nitride/$Bi_{12}O_{17}Cl_2$ composites: a promising candidate photocatalyst for boosting visible-light-driven photocatalytic degradation of tetracycline. ACS Sustainable Chem. Eng, 2018, 6: 6941−6949.

[7] Cai J, Huang J, Wang S, et al. Crafting mussel-inspired metal nanoparticle-decorated ultrathin graphitic carbon nitride for the degradation of chemical pollutants and production of chemical resources. Adv. Mater, 2019, 1806314.

[8] Liu Y, Feng Y, Yao J. Recent advances in the direct fabrication of millimeter-sized hierarchical porous materials. RSC Advances, 2016, 6(84): 80840–80846.

[9] Galarneau A, Sachse A, Said B, et al. Hierarchical porous silica monoliths: A novel class of microreactors for process intensification in catalysis and adsorption. Comptes Rendus Chimie, 2016, 19(1–2): 231–247.

[10] Cheng W, Tao K, Wu Y, et al. Preparation of hierarchical porous S-1/silica monoliths by steaming crystallization. ChemistrySelect, 2019, 4(13): 3741–3744.

[11] El Kadib A, Chimenton R, Sachse A, et al. Functionalized inorganic monolithic microreactors for high productivity in fine chemicals catalytic synthesis. Angewandte Chemie International Edition, 2009, 48(27): 4969–4972.

[12] Zhang Y, Chen Z, Liu S, et al. Size effect induced activity enhancement and anti-photocorrosion of reduced graphene oxide/ZnO composites for degradation of organic dyes and reduction of Cr(VI) in water. Applied Catalysis B: Environmental, 2013, 140: 598–607.

[13] Hao R, Wang G, Tang H, et al. Template-free preparation of macro/mesoporous g-C_3N_4/TiO_2 heterojunction photocatalysts with enhanced visible light photocatalytic activity. Applied Catalysis B: Environmental, 2016, 187: 47–58.

[14] Wang J, Tang L, Zeng G, et al. Atomic scale g-C_3N_4/Bi_2WO_6 2D/2D heterojunction with enhanced photocatalytic degradation of ibuprofen under visible light irradiation. Applied Catalysis B: Environmental, 2017, 209: 285-294.

[15] Zeng G, Zhang C, Huang D, et al. Practical and regenerable electrochemical aptasensor based on nanoporous gold and thymine-Hg 2+ -thymine base pairs for Hg 2+ detection. Biosensors and Bioelectronics, 2017, 90: 542-548.